Technical University of Denmark

DTU

Petrophysical properties of greensand as predicted from NMR measurements

Hossain, Zakir; Grattoni, Carlos A.; Solymar, Mikael; Fabricius, Ida Lykke

Link back to DTU Orbit

DTU Library
Technical Information Center of Denmark

1 **Petrophysical properties of greensand as predicted from NMR measurements**

2

3 Zakir Hossain*[1], Carlos A. Grattoni[2], Mikael Solymar[3] and Ida L. Fabricius[1]

4

5

6 [1]Department of Environmental Engineering

7 Technical University of Denmark,

8 Miljøvej, Building 113, DK-2800 Lyngby, Denmark.

9 zaho@env.dtu.dk (Zakir Hossain), ilfa@env.dtu.dk (Ida L. Fabricius)

10

11 [2]Rock Deformation Research Ltd, School of Earth and Environment

12 University of Leeds, Leeds LS2 9JT, UK, c.a.grattoni@leeds.ac.uk

13

14 [3]Statoil ASA, Oslo, Norway, miso@StatoilHydro.com

15

16 *Corresponding author (e-mail: zaho@env.dtu.dk)

17

18 Number of words of text: 7634

19 Number of references: 36

20 Number of tables: 2

21 Number of figures: 13

22

23 **Abstract**

24

25 Nuclear magnetic resonance (NMR) is a useful tool in reservoir evaluation. The objective

26 of this study is to predict petrophysical properties from NMR T_2 distributions. A series of

27 laboratory experiments including core analysis, capillary pressure measurements, NMR

28 T_2 measurements and image analysis were done on sixteen greensand samples from two

29 formations in the Nini field of the North Sea. Hermod Formation is weakly cemented,

30 whereas Ty Formation is characterized by microcrystalline quartz cement. The surface

31 area measured by BET method and the NMR derived surface relaxivity are associated

32 with the micro-porous glauconite grains. The effective specific surface area as calculated

33 from Kozeny's equation and as derived from petrographic image analysis of

34 Backscattered Electron Micrograph's (BSE), as well as the estimated effective surface

35 relaxivity is associated with macro-pores. Permeability may be predicted from NMR by

36 using Kozeny's equation when surface relaxivity is known. Capillary pressure drainage

37 curves may be predicted from NMR T_2 distribution when pore size distribution within a

38 sample is homogeneous.

39

40 **Keywords:** Greensand, glauconite, porosity, permeability, capillary pressure, NMR

41 Greensands are glauconite bearing sandstones composed of a mixture of stiff clastic

42 quartz grains and soft glauconite grains. Glauconite grains are porous and composed of

43 aggregates of iron-bearing smectitic or illitic clay. Porosity is thus found at two scales:

44 macro-porosity between grains and micro-porosity within grains (Fig. 1). Greensand

45 petroleum reservoirs occur world-wide, e.g. the mid-Cretaceous Safaniya Sandstone

46 Member in Saudi Arabia (Cagatay *et al*. 1996), the Cretaceous Mardi Greensand in

47 Australia (Hocking *et al*. 1988), the Lower Cretaceous Glauconitic sandstone in Alberta,

48 Canada (Tilley & Longstaffe 1984), the Upper Cretaceous Shannon sandstone in

49 Wyoming, USA (Ranganathan & Tye 1986), a lower Cretaceous Greensand offshore

50 Ireland (Winn 1994) and a late Paleocene Greensand in central part of the North Sea

51 (Slot-Petersen *et al*. 1998). However, evaluation of greensand reservoirs has challenged

52 geologists, engineers and petrophysicsts. Glauconite has an effect on porosity,

53 permeability and elastic properties of reservoir rocks (Diaz *et al*. 2003). Glauconite is

54 also ductile (Ranganathan & Tye 1986) so it can cause non-elastic deformation of

55 greensand (Hossain *et al*. 2009) and affect the reservoir quality. Greensands generally

56 show low resistivity in the reservoir zone due to the large amount of bound water in the

57 glauconite, yet free hydrocarbons can be produced because glauconite rather than being

58 pore-filling is part of the sand grain framework (Slot-Petersen *et al*. 1998). Core analysis

59 of greensand thus shows a poor relationship between porosity and permeability.

60 Furthermore, greensand paramagnetic glauconite or pore filling berthierine may induce

61 magnetic gradients on the pore level causing the NMR T_2 relaxation time to be shortened

62 dramatically (Rueslåtten *et al*. 1998).

63   Nuclear Magnetic Resonance (NMR) is a non-invasive technique, and NMR

64   measurements on reservoir core samples are done to obtain an improved interpretation of

65   logging data. NMR measures the net magnetization of a hydrogen atom (^{1}H) in the

66   presence of an external magnetic field. Hydrogen has a relatively large magnetic moment

67   and is abundant in both water and hydrocarbons in the pore space of a sedimentary rock.

68   NMR spectrometry involves a series of manipulations of the hydrogen protons found in

69   fluids. A measurement sequence starts with proton alignment to a magnetic field followed

70   by spin tipping, and decay. The quantities measured include signal amplitude which is

71   proportional to the number of hydrogen nuclei and decay, also called relaxation time

72   (Kenyon *et al.* 1995). Longitudinal relaxation time (T_1) measures the decay of spin

73   alignment; transverse relaxation time (T_2) measures the decay of precession. Although T_1

74   measurements are more common in the literature, they are more time consuming than T_2

75   measurements. Hence, pulsed NMR logging tools preferentially measure T_2 for faster

76   logging speeds (Straley *et al.* 1997). NMR transverse relaxation (T_2) of fluids confined in

77   a porous rock is affected by pore surface, by the bulk relaxation process in the fluid and

78   additionally by dephasing in case of molecular diffusion. T_2 may be expressed by the

79   fundamental equation governing the NMR relaxation spectrum (Coates *et al.* 1999):

80

81
$$\frac{1}{T_2} = \frac{1}{T_{2Surface}} + \frac{1}{T_{2Bulk}} + \frac{1}{T_{2Diffusion}}$$
(1)

82

83   Surface relaxation ($T_{2Surface}$) is the dominating mechanism in porous media, controlled by

84   pore surface area. The relation between NMR relaxation and pore surface area results

4

85   from strong interaction between the protons and the surface because the surface

86   relaxivity (ρ) causes rapid alignment of hydrogen protons on the pore wall, perhaps only

87   a monolayer or two thick, while protons in the remaining fluid decay through itself (bulk

88   relaxation), which is much slower (Howard *et al.* 1993). Bulk relaxation (T_{2Bulk}) is thus

89   significantly smaller than the surface relaxation and so where relaxation of diffusion

90   ($T_{2Diffusion}$) is slow, the relaxation ($\frac{1}{T_2}$) may be related to surface relaxivity and surface to

91   volume ratio of pores (*Sp*):

92

93    $$\frac{1}{T_2} = \rho_2 S_P \qquad\qquad (2)$$

94

95   NMR measurements provide information about the pore structure (*Sp*), the amount of

96   fluid in-situ and interactions between the pore fluids and surface of pores. Thus,

97   laboratory NMR measurements can be used to obtain porosity and correlate pore size

98   distribution, clay bound water, and to estimate permeability and potentially predict

99   capillary pressure curves from longitudinal relaxation time (T_1) and transverse relaxation

100   time (T_2) distribution (Kenyon 1997). Numerous authors have explored the link between

101   NMR measurements and petrophysical properties, e.g. the wettability investigation by

102   NMR measurements by Al-Mahrooqi *et al.* (2003, 2006).

103

104   Porosity is one of the key parameter for hydrocarbon reservoir evaluation, and NMR is an

105   effective tool to determine the porosity. However, several authors reported that there exist

106   significant differences between NMR porosity and core analysis porosity. Factors

107   influencing the T_2 measurements include paramagnetic minerals in the reservoir rock

108   which may cause $T_{2Diffusion}$ and hence reduce the T_2 relaxation time (Xie *et al*. 2008).

109   Aditionally, iron and other paramagnetic minerals affect the surface relaxivity and

110   produce a shift of the relaxation distribution to shorter times (Dodge *et al.* 1995).

111   Rueslåtten *et al.* (1998) studied NMR of iron-rich sandstone from the North Sea and

112   found a detrimental effect of iron bearing minerals on porosity estimation by NMR T_2.

113

114   Specific surface area is another significant petrophysical parameter for understanding the

115   physics of porous media and for permeability prediction. It was never fully integrated

116   into standard or special core analysis programs due to lack of petrophysical

117   understanding and concepts for correct evaluation (Riepe 1998). Nitrogen adsorption

118   methods (BET) yield high specific surface value as nitrogen enters the pores in the

119   sample. By using image analysis to determine the specific surface area, usually a much

120   smaller value is derived, and the value depends upon the resolution (Solymar *et al*. 2003).

121   The results of different methods reflect the different properties of pores at different

122   scales. By using a high resolution BET surface or a highly smoothed surface derived from

123   image analysis, the calculated permeability can be varied several orders of magnitude

124   (Riepe 1998). This is a concern because specific surface plays a vital role in

125   understanding and calibrating the T_2 spectra by estimating surface relaxivity (equation

126   (2)).

127

128   NMR relaxation is thus not only affected by the pore dimensions but also by the

129   relaxivity of the rock surface. Quantitative knowledge of the surface relaxivity is needed

130   when T_2 distributions are interpreted. Surface relaxivity is required in order to convert T_2

131   distribution into specific surface area, to calculate permeability and to convert T_2 time to

132   capillary pressure curves. However, to measure surface relaxivity directly is not easy.

133   Surface relaxivity may be estimated by scaling the normalized capillary pressure curve to

134   the normalized T_2 distribution (Kleinberg 1996); or by comparing NMR T_2 distributions

135   to specific surface area from nitrogen BET adsorption (Hidajat *et al*. 2002). Alternatively,

136   it can be estimated by comparing NMR pore size distribution to pore size distribution

137   from image analysis of thin sections (Howard *et al*. 1993; Kenyon 1997). Kleinberg

138   (1996) concluded that the NMR effective specific surface area is closely associated with

139   hydraulic radius of the sedimentary rock and calculated effective surface relaxivity from

140   capillary pressure curves and T_2 distribution.

141

142   Permeability is a difficult property to determine from logging data, yet it is essential for

143   reservoir characterization. Laboratory measurements provide absolute permeability at

144   core scale which could be different from reservoir permeability. NMR is the only tool

145   that attempts to estimate *in-situ* formation permeability (Hidajat *et al*. 2002; Glover *et al*.

146   2006). One of the most popular NMR derived permeability correlations is the Timur-

147   Coates formula (Coates *et al*. 1999), and is implemented as:

148

149
$$k_{NMR} = (C\phi)^m \left(\frac{FFI}{BFI} \right)^n \qquad\qquad (3)$$

150

151   where, ϕ is the porosity, *FFI* is the free fluid volume and *BFI* is the bound irreducible

152   fluid, as determined from NMR measurements. Formation dependent constants *C*, *m* and

153   *n* may be assumed to be 10, 4 and 2 for sandstones respectively, where NMR

154   permeability, k_{NMR} is given in mD. However, this equation is simply an empirical derived

155   relationship that links various NMR-derived parameters to permeability. Especially for

156   diagenetically altered consolidated reservoir rocks, the complicated internal pore

157   structures may not be described by this model, causing unrealistic permeability estimates,

158   unless empirically calibrated parameters are used, which have no general physical

159   meaning and thus are only valid for special facies types and for local investigations.

160   Timur-Coates formula also indicates that porosity or pore volume strongly controls the

161   permeability together with the effective specific surface area as expressed by $\frac{FFI}{BFI}$ in

162   accordance with the equation of Kozeny (1927). For homogeneous sediments like chalk,

163   the effective specific surface is equivalent to the one measured by nitrogen adsorption

164   (BET) and Kozeny's equation works well without introducing empirical factors

165   (Mortensen *et al*. 1998). However, for less homogenous sediments, like greensand, we

166   can calculate an effective surface area (*Sp(Kozeny)*) from permeability and porosity by

167   using Kozeny's equation. We infer that it is this effective surface that controls

168   permeability.

169

170   Capillary pressure (P_c) curves can be determined only from core analysis, but NMR

171   derived P_c curves provide a fast, cheap and non-destructive estimation. However, up to

172   now, most authors have focused on the relation between T_2 distribution and P_c curves

173   (Kleinberg 1996; Grattoni *et al*. 2003; Marschall *et al*. 1995; Volokitin *et al*. 1999) and

174   the general conclusion is that, if the bulk relaxation and diffusion effects are ignored, a

175   simple relationship between P_c and T_2 becomes:

176

177                                     $$P_c = \frac{K}{T_2}$$ (4)

178

179   where, K is an empirical scaling factor introduced to predict capillary pressure curves.

180   However, several authors, e.g. Kleinberg (1996) concluded that the match between

181   capillary pressure and NMR relaxation curves are not universal. The simple relationship

182   (equation (4)) reflects that both the T_2 distribution and P_c curves are affected by pore

183   structures but overlooks the difference between the physics of the processes. Kewan &

184   Ning (2008) discussed that in a pore and throat model of the pore space, the capillary

185   pressure is sensitive to the pore throat, whereas the NMR measures the pore body size.

186   Thus, the technique gives same information only when there is a constant ratio between

187   them.

188

189   The combination of conventional core analysis, such as Helium porosity, Gas

190   permeability, specific surface area by BET and image analysis of thin sections

191   micrographs is proven to be very effective in the evaluation of normal reservoir rocks.

192   However, for glauconite bearing greensand where a high proportion of micro-porosity in

193   glauconite grains creates an uncertainty with respect to fluid distribution and fluid

194   saturation, an accurate determination of petrophysical properties by using conventional

195   core analysis is difficult (Rueslåtten *et al*. 1998). The objective of this study is to predict

196   petrophysical properties from NMR T_2 distributions which can be applied to *in-situ* well

197   logging. Estimates of porosity, permeability, irreducible water saturation derived from

198   NMR measurement were corrected with measurements from core analysis. The porosity

199   obtained by using the different methods was compared for the greensand samples. The

200   potential use of surface area data is also described and illustrated. Kozeny's equation was

201   used for NMR permeability prediction and P_c curves were estimated from NMR

202   measurements.

203

204   **Geological setting of Nini Field**

205

206   The Nini field is located in Siri Canyon which is part of a larger system of submarine

207   canyons in the Paleocene in the Norwegian-Danish Basin running in an E-W to NE-SW

208   direction towards the Central Graben (Fig. 2) (Stokkendal *et al*. 2009). The Nini

209   accumulation is defined by a combined structural and stratigraphic trap, the anticlinal

210   structure being induced through salt tectonics. The reservoir consists of sands deposited

211   in the Siri Fairway (Schiøler *et al*. 2007).

212

213   The glauconite bearing sandstone in the Nini field was recognized by stratigraphic work

214   in Statoil in the mid-1990s (Schiøler *et al*. 2007). It is formally included in the Hermod

215   Formation and in the older Ty Formation. These Paleocene reservoir sands are

216   characterized by glauconite rich (20-30 vol %) fine grained, well sorted sand, embedded

217   in hemiplegic to pelagic mud- and marl-stones, in which both quartz grains and

218   glauconite pellets are part of the load-bearing matrix. The greensand beds thus occur in a

219   shale-sequence. In the Nini wells, the Hermod sand was found to be more massive, more

220   porous and more permeable than Ty sand (Fig. 3).

221

222   **Method**

223

224   We studied sixteen one and half inch horizontal core plugs from the two greensand

225   formations of the Nini-1 well (7 samples from Hermod Formation and 9 samples from Ty

226   Formation). The samples had already been used for routine core analysis and were chosen

227   so as to cover the range of variation in porosity (25%-40%) and air permeability (60 mD-

228   1000 mD). All cores were cleaned from brine and hydrocarbons by soxhlet extraction

229   with methanol and toluene prior to analysis. Thin sections were prepared from the end of

230   each plug and material from the end trimmings were used for X-ray diffraction (XRD)

231   and BET analysis.

232

233   **Routine core analysis**
234
235   Helium porosity (ϕ_H) of the samples was measured by the gas expansion method. Helium

236   porosity is a good measure of total porosity, including porosity in clay minerals, as no

237   pores are so small that Helium cannot enter. Buoyancy of the cores in brine (Archimedes)

238   was also used to determine bulk volume on a fully saturated sample and pore volume was

239   calculated from grain density as measured by the gas expansion method. Complete

240   saturation was verified by comparing porosity measured by Helium expansion and by

241   Archimedes method. As porosity data from the two methods are within experimental

242   error, all samples were assumed to be fully brine saturated.

243

244   Klinkenberg corrected permeability was derived from permeability at a series of nitrogen

245   gas pressures. Specific surface area of the grain (S_g) was measured by BET method by

246   using nitrogen gas adsorption. Specific surface of pores from BET method ($Sp(BET)$) was

247   calculated by dividing S_g by porous fraction, (ϕ_H) and multiplying by grain fraction, ($1-\phi_H$)

248   as:

249
$$Sp(BET) = S_g \left(\frac{1-\phi_H}{\phi_H} \right) \rho_g \qquad (5)$$

250

251   where, ρ_g is grain density.

252   The effective bulk specific surface (S) was obtained from Klinkenberg permeability (k)

253   and macro-porosity (ϕ) by using Kozeny's equation (Kozeny 1927) as:

254

255
$$k = c \frac{\phi^3}{S^2} \qquad (6)$$

256

257   where, c is Kozeny's factor which can be estimated from porosity via a simple model of

258   linear 3D interpenetrating tubes (Mortensen *et al*. 1998):

259

260
$$c = \left[4\cos\left\{ \frac{1}{3}\arccos\left(\phi\frac{8^2}{\pi^2} - 1 \right) + \frac{4}{3}\pi \right\} + 4 \right]^{-1} \quad (7)$$

261

262   According to equation (7), c increases from 0.15 to 0.25 as porosity increases from 0.05

263   to 0.5. Specific surface of pores from Kozeny's equation (*Sp(Kozeny)*) can then be

264   calculated:

265
$$Sp(Kozeny) = \frac{S}{\phi} \qquad (8)$$

266    $\dfrac{1}{Sp(Kozeny)}$ is equivalent to hydraulic radius and thus should be related to capillary

267   pressure and T_2 relaxation, so we base the remaining analysis on *Sp(Kozeny)*.

268

269   **Capillary pressure**

270

271   The capillary pressure may be expressed by the fundamental equation:

272
$$P_c = \frac{2\sigma\cos\theta}{r_c} \qquad (9)$$

273
274   where, r_c is the radius of pore throat, σ is the surface tension and θ is the contact angle.

275   For water-wet conditions *cos θ* becomes one, and in terms of specific surface of pore (*Sp*)

276   equation (9) may be rewritten as:

277

278
$$P_c = S_P\sigma \qquad (10)$$

279   Air brine drainage capillary pressure measurements were done on brine saturated

280   greensand samples by using the porous plate method at room temperature. Initially each

281   sample was saturated with simulated formation brine. The brine has a density of 1.06

282   g/cm^3 and a viscosity of 1.054 cP.   Irreducible water saturation (S_{wi}) including clay

283   bound water was determined from capillary pressure curves and macro-porosity was

284   calculated as porosity above irreducible water saturation (Fig. 4b).

285

286

287

288

289   **Image analysis**

290

291   Polished thin sections were prepared from all samples in a plane perpendicular to the

292   flow direction during core analysis. A Philips XL40 Scanning Electron Microscope was

293   used for acquisition of Back Scattered Electron (BSE) images. The images are 1024 x

294   1024 byte greyscale images with a pixel length of 1.78 µm. This magnification resolves

295   the intergranular macro-porosity and leaves the micro-porosity unresolved. Each image

296   was filtered to remove the noise and thresholded to create a binary image prior to

297   analysis. Porosity determined in the images is called image porosity (ϕ_{image}). The image

298   analysis procedure is sensitive to porosity threshold, so image porosity was determined when

299   they are equal to macro-porosity determined from P_C measurements. The macro-porosity

300   determined by image analysis is within a narrow range (±2.5 p.u.) obtained by image analysis

301   along. The specific surface area or strictly speaking the specific perimeter (*S(image)*) of

302   the solid grains was determined by using the method of Borre *et al.* (1995). According to

303   Underwood (1970) and Solymar & Fabricius (1999) the specific perimeter (*S(image)*) may

304   be approximated to the 3-D specific surface (*S)* by:

305

306                           $$S = \frac{4}{\pi} S(image) \qquad\qquad (11)$$

307

308   Image specific surface of pores (*S_p (image)*) is thus calculated by using equation (8) where

309   porosity is defined as macro-porosity determined from capillary pressure measurements.

310

311   **NMR measurements**

312

313   For NMR measurements all samples were saturated with brine (7.6 % NaCl). Complete

314   saturation was verified by using the dry weight, the saturated weight, grain volume by

315   Helium expansion, and brine density. All samples attained full brine saturation. All the

316   measurements were performed with the samples sleeved in PTFE heat shrink as several

317   were poorly consolidated. The weights and volumes of the heat shrink material were

318   accounted for in the measurements.

319

320   The laboratory NMR measurements were performed using a Resonance Instruments

321   MARAN 2 spectrometer at ambient pressure and 34°C at a proton resonance frequency of

322   2.2 MHz. T_2 relaxations was measured using Carr-Purcel-Meiboom-Gill (CPMG) pulse

323   sequence. The T_2 relaxation curves were measured by using a Recycle Delay (Repetition

324   Time) of 10 sec, Number of Echos 8000, CPMG inter echo spacing (τ) 200 μs and 100

325   scans. The $\pi/2$ and π pulses were 14.8μs and 29.6μs, respectively.

326

327   NMR porosity of the fully saturated samples was determined by using the total signal

328   amplitude of each sample (by summing the amplitudes of the T2 distribution) and known

329   standard of similar diameter. In this case the reference standard was a sealed glass vial,

330   containing $3cm^3$ of 50,000 ppm NaCl and $17cm^3$ of deuterium oxide. Deuterium oxide

331   does not have an NMR signal therefore this reference standard has an equivalent porosity

332   of 15%. The same number of scans was used for the reference and the sample. NMR

333   porosity is then calculated using the, total signal amplitude, the bulk volume, hydrogen

334   index of both plug and reference and the equivalent porosity of the reference.

335

336   For determining the macro-porosity and micro-porosity we need a cutoff value from the

337   T_2 distribution. For two samples (one from Hermod and one from Ty), the T_2 cutoff was

338   determined in the laboratory by obtaining the T_2 distribution at two saturations, fully

339   brine saturated and at irreducible water saturation as determined from capillary pressure

340   curves. The analysis of the air-water systems is relatively easy as there is no NMR

341   response from the air and the relaxation time is exclusively due to the protons in the

342   water. The cutoff time is defined as the relaxation time at the point where the cumulative

343   porosity of the fully saturated sample equals the irreducible water saturation (Fig. 4a). As

344   the T_2 cutoff is determined from capillary pressure equilibrium experiments includes

345   capillary bound fluid and trapped in micro-pores. A single T_2 cutoff value for each

346   formation was used for all samples of that formation. The cumulative porosity over the

347   range $T_2 > T_{2cutoff}$ was the macro-porosity and below the range $T_2 < T_{2cutoff}$ was the micro-

348   porosity or irreducible water saturation.

349

350   The NMR permeability model used in this work was obtained by combining equation (2),

351   (6), and (8):

352

353    $$k = c\phi(T_2\rho_2)^2 \qquad\qquad (12)$$

354

355   In a similar way the capillary pressure NMR model was obtained combining equation (2)

356   and (10):

357    $$P_c = \frac{\sigma}{\rho_2 T_2} \qquad\qquad (13)$$

358   The assumption of this model is that: 1- the pore structure controlling the T2 distribution

359   and capillary pressure is a bundle of capillary tubes and the drainage is controlled by the

360   hierarchy of pore sizes; 2- the surface relaxivity is constant overall the sample; 3-

361   diffusion relaxation is negligible.

362

363   **Results**

364

365   The Helium porosity of greensand ranges from 28 to 42 p.u. (porosity units) with a

366   maximum uncertainty 1.5 p.u. (Table 1). Klinkenberg corrected permeability ranges from

367   60 to 940 mD (Table 2). Permeabilities of Hermod samples are larger than Ty samples

368   and correlates with porosity, whereas Ty data are more scattered (Fig. 5).

369

370   Petrographic thin section analysis indicates that the studied Paleocene greensands are

371   well to very well sorted, dominated by grains of quartz but also large volumes of

372   glauconite (20-25 vol %) (Fig. 6). Samples from Hermod Formation contain glauconite

373   grains of size between 100 and 200 µm, some glauconite grains are larger (300 to 400

374   µm) (Fig. 1a). Samples from Ty Formation contain glauconite grains of size between 100

375   and 150 µm, although some glauconite grains are larger (200 to 300 µm) (Fig. 1b). The

376   grains are subangular to sub-rounded for the both Formations. Hermod Formation is only

377   weakly cemented, whereas samples from Ty formation contain cement of berthierine or

378   microcrystalline quartz cement resulting in relative in a low permeability (Table 2). In

379   both formations XRD analyses of separated glauconite grains show the presence of some

380   expanding layers in the predominantly illitic glauconite.

381

382   The capillary pressure was obtained assuming 72 mN/m for the brine surface tension.

383   Capillary pressure curves show that for the higher permeability Hermod Formation

384   samples, the P_c curves are shifted toward low irreducible water saturation, whereas P_c

385   curves for the lower permeability Ty Formation samples are shifted toward high

386   irreducible water saturation (Figs 7a, c). Irreducible water saturation from capillary

387   pressure was obtained at P_c 100 psi, and varied between 25% and 42% of the total

388   porosity (Table 2).

389

390   The NMR T_2 distributions are presented in graphical form for each sample and the

391   population is expressed in porosity units in Figures 7b, d. All T_2 distributions are

392   bimodal. Each T_2 time corresponds to a particular pore size. If the rock has a single pore

393   size then instead of a broader distribution there will be a single vertical line. Thus broader

394   distributions reflect greater variability in pore size. We have determined a time cutoff of

395   5.21 ms for the sample 1-4 from Hermod Formation and 3.68 ms for sample 1A-141 from

396   the Ty Formation. The short relaxation time component in a T_2 distribution of a rock is

397   attributed to the water in glauconite. For the present greensand samples a peak close to 1

398   ms should correspond to glauconite water, whereas all samples also present a second

399   peak close to 100 ms that corresponds to movable fluid. Higher permeability Hermod

400   Formation samples show larger amplitude in the movable fluid than samples from Ty

401   Formation; whereas lower permeability bearing Ty Formation sample show slightly

402   larger amplitude in capillary bound and glauconite water (Figs 7b, d).

403

404   **Discussion**

405   **Porosity**

406

407   Helium porosity, Archimedes porosity and NMR porosity are compared in Figure 8.

408   Helium porosity is associated with the total porosity of the sample including micro-

409   porosity in glauconitic and it shows the highest values among the three types of porosity

410   data. However, Archimedes and NMR porosity should also in principle represent the total

411   porosity of a sample, but could be lower if water saturation is below 100%. Although the

412   Archimedes porosity is close to Helium porosity, NMR porosity tends to be lower. Both

413   macro-porosity and micro-porosity are underestimated by the NMR measurements (Figs

414   8c, d). The discrepancy between Archimedes porosity and NMR porosity could be due to

415   several factors. First, NMR and Archimedes porosity depend on saturation condition of

416   the sample. So we cannot rule out that during NMR measurement the saturation condition

417   was lower than that at the Archimedes measurements. Second, paramagnetic iron-bearing

418   minerals in reservoir rock may be an important factor influencing T_2 measurements as

419   shown by Dodge *et al.* (1995). The presence of paramagnetic ions increases the rate of

420   relaxation of the hydrogen proton. This is expected for greensand because glauconite and

421   berthierine are iron-bearing. These clay minerals have large surface area and high

422   magnetic susceptibilities leading to large internal gradients and short T_2 (Straley *et al*.

423   1997). Rueslåtten *et al.* (1998) illustrated the influence of chlorite (berthierine) and

424   glauconite on the difference between Helium porosity and NMR T_2 derived porosity

425   (delta porosity) and found broad positive correlation between delta porosity and chlorite

426   content, whereas they found no correlation with glauconite content. Thus they pointed to

427   the detrimental effect of chlorite or berthierine on porosity estimated by NMR. However,

428   we found only a vague negative correlation between delta porosity and bulk mineral

429   composition (glauconite, clay coating and pores filling) (Fig. 8b).

430

431   **Specific surface area**

432

433   Specific surface area with respect to pore (*Sp*), determined by three methods are

434   compared in Figure 10a. We found a large difference between the specific surface areas

435   as measured by BET method (*Sp(BET),* 76-141 µm^{-1}) and calculated by Kozeny's

436   equation (*Sp(Kozeny),* 0.27-0.95 µm^{-1}) and determined by image analysis (*Sp(image),*

437   0.32-0.46 µm^{-1}). Nitrogen adsorption has a very high resolution; therefore this method

438   determines the specific surface of the total porosity, including micro-porosity. Based on

439   the Kozeny's equation, we estimated *Sp(Kozeny)* by using permeability determined on

440   the cores and macro-porosity. *Sp* by image analysis depends on the resolution of the

441   image (Solymar *et al*. 2003). However, *Sp* from image analysis at the present pixel size

442   and *Sp* from Kozeny's equation are in same order of magnitude which tells us that

443   resolution of image is sufficient and pixel size is small enough to determine *Sp* by image

444   analysis. The specific surface area of separated glauconite grains are in order of 1300-

445   1600 µm^{-1}, whereas the specific surface area of quartz grains is less than 1 µm^{-1}. So

446   rather than quartz grains, specific surface of glauconite grains are measured by BET

447   method. Thus, *Sp* by BET method is mainly reflected by the micro-pores of glauconite

448   grains and pore filling/lining clays, whereas *Sp* from Kozeny's equation and image

449   analysis is associated with effective surface and related to macro-porosity. We found that

450   *Sp* measured by BET method is well correlated with fraction of glauconite plus pore

451   filling clay minerals (Fig. 9c).

452

453   We found that irreducible water saturation ranges from 22% to 41% from capillary

454   pressure measurements and from 23% to 36% from NMR measurements. Considering

455   errors association with these two methods, irreducible water saturations are close to each

456   other. The high value of irreducible water saturation is due to the high specific surface of

457   glauconite. The micro-pores of glauconite remain brine filled even at a capillary pressure

458   of 100 psi. We found a positive correlation between irreducible water saturation

459   determined from P_c and NMR with *Sp* determined from BET method (Figs 9a, b). In

460   addition Figures 9a, b also show the tendency for low surface area samples to approach

461   minimum irreducible water saturation and for high surface area samples to remain more

462   saturated. A relationship between specific surface and irreducible water saturation has

463   been noted by several authors e. g. Hamada *et al.* (2001) where authors reported an

464   excellent correlation (R^2=0.98) between irreducible water saturation and specific surface

465   of pores.

466

467   **Surface relaxivity**

468

469   We compare four ways of estimating surface relaxivity in Figure 10b. Equation (2) shows

470   that surface relaxivity for NMR T_2 distribution is related to specific surface of pores.

471   Thus in absence of laboratory data, surface relaxivity may be evaluated by comparing T_2

472   distributions with *Sp(BET)*, *Sp(Kozeny)* or *Sp(image)*. This results in relaxivity value

473   ranges in order of 2.7-4.2 µm/s from *Sp(BET)*, 7-58 µm/s from *Sp(Kozeny)*, and 10-35

474   µm/s from *Sp(image)*. As an alternative, we used P_c curves and found that a surface

475   relaxivity of 20.4 µm/s for Hermod and of 28.4 µm/s for Ty Formation are needed to

476   generate Pc curves from NMR measurements. The surface relaxivity estimated based on

477   *Sp(BET)* would be controlled by micro-porosity in glauconite. We found an average

478   surface relaxivity by *Sp(BET)* of 3.42 µm/s, which is close to the 3.3 µm/s for glauconite

479   reported by Matteson et al. (1996). Surface relaxivity estimated from *Sp(Kozeny)* and

480   *Sp(image)* also should be effective surface relaxivity as it was calculated from effective

481   specific surface area.

482

483   **Permeability**

484

485   Kozeny's equation (equation (12)) was used to predict permeability from NMR T_2

486   distributions. Before applying this equation we highlight the similarities and differences

487   within T_2 distribution among samples (Fig. 11). The T_2 distribution of sample 1-18 peaks

488   at longer time than for sample 1-6, thus the larger porosity of sample 1-18 is due to the

489   larger pores which also cause higher permeability (Fig. 11a). The comparison of three

490   samples with similar distributions at shorter times is shown in Figure 11b. When the

491   larger peak (around 100 ms) becomes smaller and is shifted to larger times due to a small

492   number of intermediate pores, there is a small increase of the number of larger pores.

493   Thus, for these samples the permeability is not high although porosity is higher. We thus

494   cannot use average T_2 time or final T_2 time in equation (12) for permeability calculation.

495   So we modified the equation (12) by summing the total permeability among the T_2

496   distribution and only including the macro-porosity. Thus resulting:

497

498    $$k = c\phi\rho_2^2 \sum_{i=1}^{N} f_i (T_{2i})^2 \qquad (14)$$

499

500   where, *fi* is a fraction of the total amplitude of each T_{2i}. Kozeny factor c was calculated

501   using equation (7).

502

503   The predicted permeability distribution obtained by using equation (14) is shown in

504   Figures 11c, d. Below cutoff time, the amplitude of permeability is zero which means

505   micro-porosity does not contribute to fluid flow. From cutoff time to 100 ms, the

506   amplitude of permeability is small but above 100 ms the contribution of permeability

507   increases.

508

509   Predicted permeability and measured permeability are compared in Figure12a by using

510   surface relaxivity from *Sp(Kozeny)* (Average surface relaxivity for each depth interval),

511   in Figure 12b by using surface relaxivity from *Sp*(image), in Figure 12c by using surface

512   relaxivity from equation (13), and in Figure12d by using surface relaxivity from *Sp(BET)*.

513   Predicted permeability is close to 1:1 line of measured permeability for case 1 and 2. The

514   estimated permeability from Timur-Coates model is illustrated in Figure 12e. Predicted

515   permeability using this model works rather well if we use *C*=8.3 which was optimized in

516   a least-squares sense such that the sum of the squared error between the measured and

517   predicted permeability is minimized. Predicted permeability from image analysis and

518   measured permeability are compared in Figure 12f. Image permeability and NMR

519   predicted permeability by using surface relaxivity from *Sp*(image) are equal.

520

521   **Capillary pressure curves**
522

523   We applied the value of surface relaxivity of 20.3 µm/s and 28.4 µm/s for Hermod

524   Formation and Ty Formation sample respectively to generate the capillary pressure

525   curves directly from the T_2 distribution by using equation 13 (Fig. 13). Capillary

526   pressure curves overlay each other for low permeability samples. However, we found

527   deviation between the P_c NMR and P_c lab for the high permeability sample from Hermod

528   Formation. A deviation is to be expected,   because we assumed uniform surface

529   relaxivity within a sample and ignored diffusion relaxation. The calculated surface

530   relaxivity is shown in Figure 13e for a sample from Hermod Formation and in Figure 13f

531   for a sample from Ty Formation. A good match between P_c curves from laboratory and

532   NMR measurement is found when average surface relaxivity is equal to surface relaxivity

533   applied to predict P_c curves from NMR. In contrast, we found deviation between P_c

534   curves from laboratory and NMR measurements when average surface relaxivity is not

535   equal to the surface relaxivity need to match Pc curves. This variation of surface

536   relaxivity within the sample is probably due to the large pores and higher permeability in

537   the greensands of Hermod Formation.

538

539   **Conclusion**

540
541   The objective of this study is to predict petrophysical properties from NMR T_2

542   distributions. Based on laboratory experiments and image analysis on sixteen greensand

543   samples from the two formations in the Nini field of the North Sea, we found Hermod

544   Formation is only weakly cemented, whereas samples from Ty formation contain cement

545   of berthierine or microcrystalline quartz cement resulting in relatively to lower

546   permeability than Hermod samples.

547

548   We found that the total porosity measured by Archimedes method is to close to Helium

549   porosity, whereas NMR porosity tends to be lower. The discrepancy between Archimedes

550   porosity and NMR porosity may be due to a combination of several factors, including the

551   presence of glauconite grains in greensand.

552

553   This study shows that the surface area measured by BET method and the derived surface

554   relaxivity are associated with the micro-porous glauconite grains. The effective surface

555   area as calculated by Kozeny's equation and as determined from petrographic image

556   analysis of Backscattered Electron Micrographs and the estimated effective surface

557   relaxivity is associated with macro-pores. We found that *Sp* measured by BET method is

558   well correlated with fraction of glauconite plus pore filling clay minerals.

559

560   Irreducible water saturation in the studied greensands ranges from 22% to 41% and these

561   high values are due to the high specific surface area of glauconite. The micro-pores of

562   glauconite remain brine filled even at a capillary pressure of 100 psi.

563

564   We found that predicted permeability from NMR by using Kozeny's equation agrees well

565   when surface relaxivity is known. By using Timur-Coates model, predicting permeability

566   works rather well if we optimize the constant to *C*=8.3.

567

568   This study shows that predicted capillary pressure curves from NMR T_2 distribution

569   overlay on measured capillary pressure curves for low permeability samples. The

570   deviation between the P_c NMR and P_c lab for the high permeability samples is due to the

571   contrasting relaxivity on the surface of quartz and glauconite.

572

573   **Acknowledgements**

574

579

580   **Appendix**

581   **Nomenclature**

582   *BFV*   Bound fluid volume

583   *C*   Formation dependent constant

584   *c*   Kozeny factor

585   f_i Amplitude of each T_{2i}

586   *FFI*   Free fluid volume

587   *k*   Klinkenberg permeability,

588   *K*   Scaling factor

589   *S*   Specific surface area of bulk

590   S_g Specific surface area of grains

591   *Sp*   Specific surface of pores

592   T_{2Bulk} Relaxation of fluids

593    $T_{2Diffisionk}$ Relaxation of molecular diffusion

594    $T_{2Surface}$ Relaxation of surface

595

596   **Greek symbols**

597   ϕ Porosity (fraction)

598   ρ Surface relaxivity

599   τ Inter echo spacing.

600

601   **Unit conversion**

602

603   $1 \text{ mD} = 0.9869 \text{ } 10^{-15} \text{ m}^2$

604   1 psi = 6.89 kPa

605

606   **References**

607

608   Al-Mahrooqi, S. H., Grattoni, C. A., Muggeridge, A. H., Zimmerman, R. W. & Jing, X.

609   D. 2006. Pore-scale modeling of NMR relaxation for the characterization of wettability.

610   *Journal of Petroleum Science and Engineering,* **52**, 172-186.

611   Al-Mahrooqi, S. H., Grattoni, C. A., Moss, A. K. & Jing, X. D. 2003. An investigation of

612   the effect of wettability on NMR characteristics of sandstone rock and fluid systems.

613   *Journal of Petroleum Science and Engineering,* **39**, 389-398.

614   Borre, M., Lind, I. & Mortensen, J. 1997. Specific surface as a measure of burial

615   diagenesis of chalk. *Zentralblatt fur Geologie und Palaontologie,* **1**, 1071–1078.

616   Cagatay, M. N., Saner, S., Al-Saiyed, I. & Carrigan, W. J. 1996. Diagenesis of the

617   Safaniya Sandstone Member (mid-Cretaceous) in Saudi Arabia. *Sedimentary Geology,*

618   **105**, 221-239.

619   Coates, G. R., Xiao, L., et al. 1999. *NMR logging principles and applications*. Gulf

620   Professional Publishing, Houston, Texas, 234.

621   Diaz, E., Prasad, M., Mavko, G. & Dvorkin, J. 2003. Effect of glauconite on the elastic

622   properties, porosity, and permeability of reservoir rocks. *The Leading Edge,* **22**, 42-45.

623   Dodge, W. S., Shafer, J. L., Guzman-Garcia, A. G., & Noble, D. A. 1995. Core and Log

624   NMR Measurements of an Iron-Rich, Glauconitic Sandstone Reservoir. *36th Annual*

625   *Symposium of SPWLA*, Paris, France, June 26-29.

626   Glover, P., Zadjali, I. & Frew, K. 2006. Permeability prediction from MICP and NMR

627   data using an electrokinetic approach. *Geophysics,* **71**, 49-60.

628   Grattoni, C. A., Al-Mahrooqi, S. H., Moss, A. K., Muggeridge, A. H. & Jing, X. D. 2003.

629   An improved technique for deriving drainage capillary pressure from NMR T_2

630   distributions. *The International Symposium of the Society of Core Analysis,* **25,** 21-24

631   September, Pau, France.

632   Hamada, G., Al-Blehed, M., Al-Awad, M. & Al-Saddique, M. 2001. Petrophysical

633   evaluation of low-resistivity sandstone reservoirs with nuclear magnetic resonance log.

634   *Journal of Petroleum Science and Engineering,* **29**, 129-138.

635   Hidajat, I., Singh, M., Cooper, J. & Mohanty, K. K. 2002. Permeability of porous media

636   from simulated NMR response. *Transport in Porous Media,* **48**, 225-247.

637   Hocking, R., Voon, J. & Collins, L. 1988. Stratigraphy and sedimentology of the basal

638   Winning Group, northern Carnarvon Basin. In: P.G. Purcell and R.R. Purcell (editors),

639   The North West Shelf, Proceedings of Petroleum Exploration Society Australia

640   Symposium, Perth, 203–224.

641   Hossain, Z., Fabricius, I. L. & Christensen, H. F. 2009. Elastic and nonelastic

642   deformation of greensand. *The Leading Edge,* **28**, 260-262.

643   Howard, J. J., Kenyon, W. E. & Straley, C. 1993. Proton magnetic resonance and pore

644   size variations in reservoir sandstones. *SPE Formation Evaluation,* **1**, 194-200.

645   Kenyon, B., Kleinberg, R., Straley, C. & Morriss, C. 1995. Nuclear Magnetic Resonance

646   Imaging—Technology for the 21st Century. *Oilfield Review,* **7**, 19–30.

647   Kenyon, W. E. 1997. Petrophysical principles of applications of NMR logging. *The Log*

648   *Analyst,* **38**, 21-43.

649   Kewan, W. & Ning, L. 2008. Numerical simulation of rock pore-throat structure effects

650   on NMR T2 distribution. *Applied Geophysics,* **5**, 86-91.

651   Kleinberg, R. 1996. Utility of NMR T_2 distributions, connection with capillary pressure,

652   clay effect, and determination of the surface relaxivity parameter ρ_2. *Magnetic resonance*

653   *imaging,* **14**, 761-767.

654   Kozeny, J. 1927. Ueber kapillare Leitung des Wassers im Boden.

655   *Sitzungsber.Akad.Wiss.Wien,* **136**, 271-306.

656   Marschall, D., Gardner, J. S., Mardon, D. & Coates, G. R. 1995. Method for correlating

657   NMR relaxometry and mercury injection data. *Proceeding of the 1995 International*

658   *Symposium of Society of core Analysts,* papers 9511.

659   Mortensen, J., Engstrøm, F. & Lind, I. 1998. The relation among porosity, permeability,

660   and specific surface of chalk from the Gorm field, Danish North Sea. *SPE Reservoir*

661   *Evaluation and Engineering,* **1**, 245-251.

662   Ranganathan, V. & Tye, R. S. 1986. Petrography, diagenesis, and facies controls on

663   porosity in Shannon Sandstone, Hartzog Draw Field, Wyoming. *AAPG Bulletin,* **70**, 56-

664   69.

665   Riepe, L. 1998. Specific internal surface: the "forgotten?" petrophysical measurement!

666   *Proceeding of the 1998 International Symposium of Society of core Analysts,* papers

667   9540.

668   Rueslåtten, H., Eidesmo, T., Lehne, K. A. & Relling, O. M. 1998. The use of NMR

669   spectroscopy to validate NMR logs from deeply buried reservoir sandstones. *Journal of*

670   *Petroleum Science and Engineering,* **19**, 33-44.

671   Rueslåtten, H., Eidsemo, T. & Slot-Petersen, C. 1998. NMR studies of iron-rich

672   sandstone oil reservoir. *Proceeding of the 1998 International Symposium of Society of*

673   *core Analysts,* papers 9821

674   Schiøler, P., Andsbjerg, J., Clausen, O. R., Dam, G., Dybkjær, K., Hamberg, L.,

675   Heilmann-Clausen, C., Johannessen, E. P., Kristensen, L. E. and Prince, I., 2007.

676   *Lithostratigraphy of the Paleocene: Lower Neogene succession of the Danish North Sea.*

677   Geological Survey of Denmark and Greenland, Danish Ministry of the Environment

678   report 77.

679   Slot-Petersen, C., Eidsemo, T., White, J. & Rueslatten, H. G. 1998. NMR formation

680   evaluation application in a complex low resistivity hydrocarbon reservoir. *Transactions*

681   *of the SPWLA 39th Annual Logging Symposium*, Paper 1998-TT

682   Solymar, M. & Fabricius, I. L. 1999. Image analysis and estimation of porosity and

683   permeability of Arnager Greensand, Upper Cretaceous, Denmark. *Physics and Chemistry*

684   *of the Earth Part A-Solid Earth and Geodesy, 24*, 587-591.

685   Solymar, M., Fabricius, I. L. & Middleton, M. 2003. Flow characterization of glauconitic

686   sandstones by integrated Dynamic Neutron Radiography and image analysis of

687   backscattered electron micrographs. *Petroleum Geoscience, 9*, 175-183.

688   Stokkendal, J., Friis, H., Svendsen, J. B., Poulsen, M. L. K. & Hamberg, L. 2009.

689   Predictive permeability variations in a Hermod sand reservoir, Stine Segments, Siri Field,

690   Danish North Sea. *Marine and Petroleum Geology, 26*, 397-415.

691   Straley, C., Roosini, D., Vinegar, H., Tutunjian, P. & Morriss, C. 1997. Core analysis by

692   low-field NMR. *The Log Analyst, 38*, 84-94.

693   Tilley, B. J. & Longstaffe, F. J. 1984. Controls on hydrocarbon accumulation in

694   glauconitic sandstone, Suffield heavy oil sands, southern Alberta. *AAPG Bulletin, 68*,

695   1004-1023.

696   Underwood, E. E. 1970. *Quantitative stereology*. Addison -Wesley, Reading,

697   Massachusetts, 270.

698   Volokitin, Y., Looyestijn, W. J., Slijkerman, W. F. J. & Hofman, J. P. 1999. A Practical

699   Approach to Obtain 1st Drainage Capillary Pressure Curves From NMR Core and Log

700   Data. *The International Symposium of the Society of Core Analysts, 24*, 1–4.

701   Winn, R. D. 1994. Shelf Sheet-Sand Reservoir of the Lower Cretaceous Greensand,

702   North Celtic Sea Basin, Offshore Ireland. *AAPG Bulletin,* **78**, 1775-1789.

703   Xie, R. H., Xiao, L. Z., Wang, Z. D. & Dunn, K. J. 2008. The influence factors of NMR

704   logging porosity in complex fluid reservoir. *Science in China Series D: Earth Sciences,*

705   **51**, 212-217.

706

707   **Figure captions**

708

709   **Fig. 1.** BSE images of greensand samples. (a) Sample 1-4 from Hermod Formation and

710   (b) sample 1A-142 from Ty Formation. Scale bar is 200 µm. Q: quartz; Gl: glauconite; H:

711   Heavy minerals, M: Mica; PF: pore filling clay minerals. Porosity, permeability and

712   irreducible water saturation are 37 p.u., 530 mD and 26% for sample 1-4 and 29 p.u., 150

713   mD and 38% for sample 1A-142.

714

715   **Fig. 2.** Location map showing the position of the Nini-1 well used in this study (arrow).

716   The margins of the Siri Canyon are shown by grey shading. An area of positive relief

717   within the canyon is also shown by grey shading. G, Germany; N, Norway; NL,

718   Netherlands; S, Sweden; UK, United Kingdom (Figure modified after Schiøler *et al*.

719   2007).

720

721   **Fig. 3.** Gamma ray, porosity and resistivity logs for wells Nini-1 (top) and Nini-1A

722   (bottom). The glauconite bearing reservoir intervals (Hermod sand and Ty sand) have

723   relatively low separation between neutron- and density porosity. Horizontal dashed lines

724   indicate the studied core intervals. Core data are shown for reference. Permeability is

725   higher in Hermod sand than in Ty sand.

726

727   **Fig. 4**: Macro-porosity and micro-porosity determination for sample 1-4 (a) from NMR

728   T_2 distribution (b) from the capillary pressure curve. The cumulative distribution for the

729   fully saturated sample is compared to the cumulative distribution after centrifuging at 100

730   psi. The cutoff time which separates the T_2 distribution into macro-porosity and micro-

731   porosity is defined as the relaxation time at the point where the cumulative porosity of the

732   fully saturated sample equals the irreducible water saturation. The dashed vertical line is

733   shown a cutoff of 5.21 ms. The capillary pressure of 100 psi corresponds to a micro-

734   porosity of 9.1%.

735

736   **Fig. 5.** Cross plot of macro-porosity from capillary pressure measurement and

737   permeability. Samples from the Hermod sand have similar porosity and permeability,

738   whereas the samples from Ty sand are more scattered. The reference lines represent equal

739   specific surface of pores (*Sp (Kozeny)*) in μm^{-1} as calculated by using Kozeny's equation.

740   The data indicate that *Sp* is lower in Hermod sand than in Ty sand.

741

742   **Fig. 6.** Bulk composition of investigated samples from Hermod and Ty Formations of the

743   Nini Field. Mineral composition was determined by point counting of 500 points across

744   each entire thin-section. Macro-porosity was determined by image analysis when porosity

745   threshold is equal to macro-porosity determined from P_c measurements. Micro-porosity is

746   the difference between Helium porosity and image porosity.

747

748   **Fig. 7.** (a), (c) Capillary pressure curves and (b), (d) NMR T_2 distribution curves of

749   greensand samples. (a) P_c curves of Hermod Formation samples are shifted toward low

750   irreducible water saturation, whereas (c) the Ty Formation samples have relatively high

751   irreducible water saturation. This pattern compares to the relatively high permeability of

752   Hermod sand relative to the low permeability of Ty sand (Fig. 3). T_2 distribution of all

753   samples shows two peaks. The peak close to 1 ms represents micro-porosity and the peak

754   close to 100 ms represents macro-porosity.

755

756   **Fig. 8.** (a) Helium porosity, Archimedes porosity and NMR porosity of investigated

757   samples. Helium porosity tends to be the highest, whereas NMR porosity is

758   underestimated due to iron bearing minerals in greensand. (b) Cross plot of delta porosity

759   (Archimedes porosity-NMR porosity) and minerals bulk composition (glauconite, pore

760   filling clay and clay coating). Cross plots of (c) macro-porosity and (d) micro-porosity

761   from NMR T_2 distribution and capillary pressure curves.

762

763   **Fig. 9.** Correlation between specific surface of pores as measured by BET (*Sp (BET)*) and

764   (a) irreducible water saturation as determined from NMR measurements, (b) irreducible

765   water saturation as determined from capillary pressure measure as well as (c) clay

766   minerals (glauconite, clay coating and pore filling clay) as percentage of bulk

767   composition.

768

769   **Fig. 10.** (a) Specific surface area with respect to pore (*Sp*) determined by BET nitrogen

770   adsorption (*Sp (BET)*), estimated from Kozeny's equation (*Sp (Kozeny)*) and determined

771   by image analysis of the BSE images (*Sp (image)*). (b) Surface relaxivity determined

772   comparing T_2 distribution with *Sp (BET)*, *Sp (Kozeny)*, and *Sp (image)*. For two samples,

773   surface relaxivity are also determined from capillary pressure versus NMR T_2

774   distribution.

775

776   **Fig. 11.** (a), (b) Porosity distribution and cumulative porosity for five greensand samples.

777   (c), (d) Permeability distribution of five greensand samples obtained from Kozeny's

778   equation.

779

780   **Fig. 12.** Measured permeability versus NMR predicted permeability by using surface

781   relaxivity from (a) *Sp(Kozeny)*, (b) *Sp(image)*, (c) *Sp(BET)*, (d) P_c versus NMR and (e)

782   from Timur-Coates model. (g) Measured permeability versus predicted permeability from

783   image analysis. Image permeability and NMR predicted permeability by using surface

784   relaxivity from *Sp(image)* are equal.

785

786   **Fig. 13.** Air Brine capillary pressure curves including saturation error compared with

787   NMR derived capillary pressure including saturation error. Saturation error corresponds

788   to the error associated with porosity measurements. The NMR derived capillary pressure

789   curves are based on surface relaxivity value of 20.4 µm/s for Hermod Formation and 28.4

790   µm/s for Ty formation. Deviation between average surface relaxivity (solid line) and

791   surface relaxivity for predicting P_c NMR (dashes line) are shown (e) for Hermod

792   Formation and (f) for Ty Formation.

793

794   **List of tables**

795

796   Table 1. *Core plug porosity data. Helium porosity was measured by Helium gas*

797   *expansion, Archimedes porosity was measured by immersing, and NMR porosity was*

798   *measured by the signal amplitude of T_2 measurements respectively. Archimedes macro-*

799   *porosity and NMR macro-porosity were determined from capillary pressure curves and*

800   *T_2 distributions respectively.*

801

802   Table 2. *Core plug data. Specific surface area of grains (SSA) was measured by BET*

803   *method and effective specific surface of pores (Sp(Kozeny)) was calculated by using*

804   *Kozeny's equation. Image specific perimeter of pores (Sp(image)) was determined by*

805   *image analysis by using the method of Borre et al. (1997). The cutoff time which*

806   *separates the T_2 distribution into macro-porosity and micro-porosity is defined as the*

807   *relaxation time at the point where the cumulative porosity of the fully saturated sample*

808   *equals the irreducible water saturation.*

Fig. 1

(a) (b)

Fig. 2

Fig. 3

(a) (b) (c) (d)
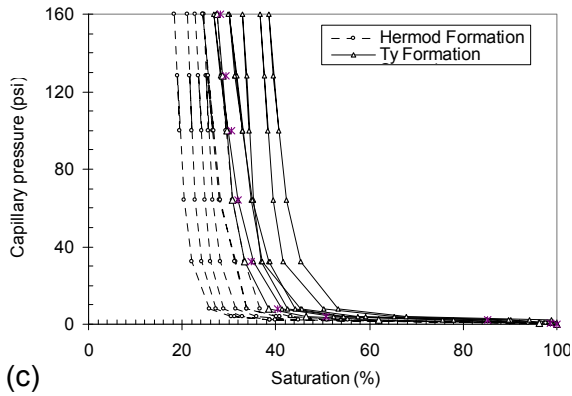
(e) (f) (g) (h)

Fig. 4

(a)

(b)

Fig. 5

Fig. 6

Fig. 7

(a)

(b)

(c)

(d)

Fig. 8

(a)

(b)

(c)

(d)

Fig. 9

(a)

(b)

(c)

Fig. 10

(a)

(b)

Fig. 11

(a)

(b)

(c)

(c)

Fig. 12

(a) ρ_2 (Kozeny)

(b) ρ_2 (image)

(c) ρ_2 (Pc vs. NMR)

(d) ρ_2 (BET)

(e) Timur-Coates model

(f)
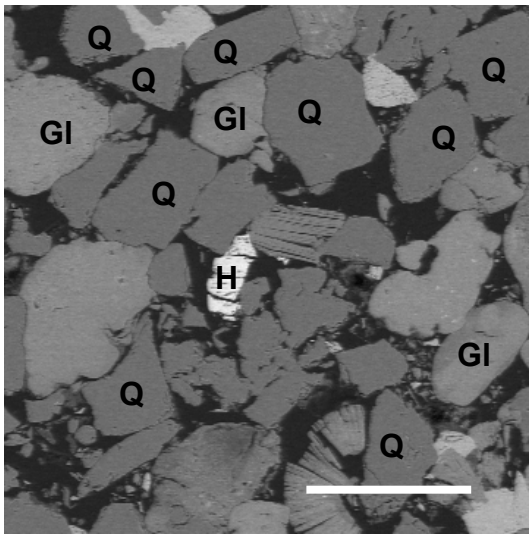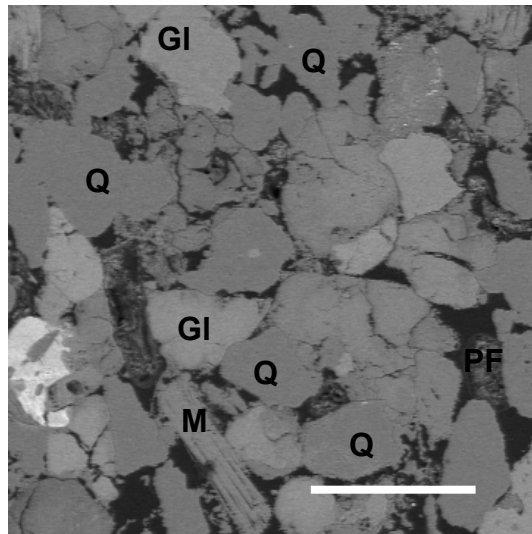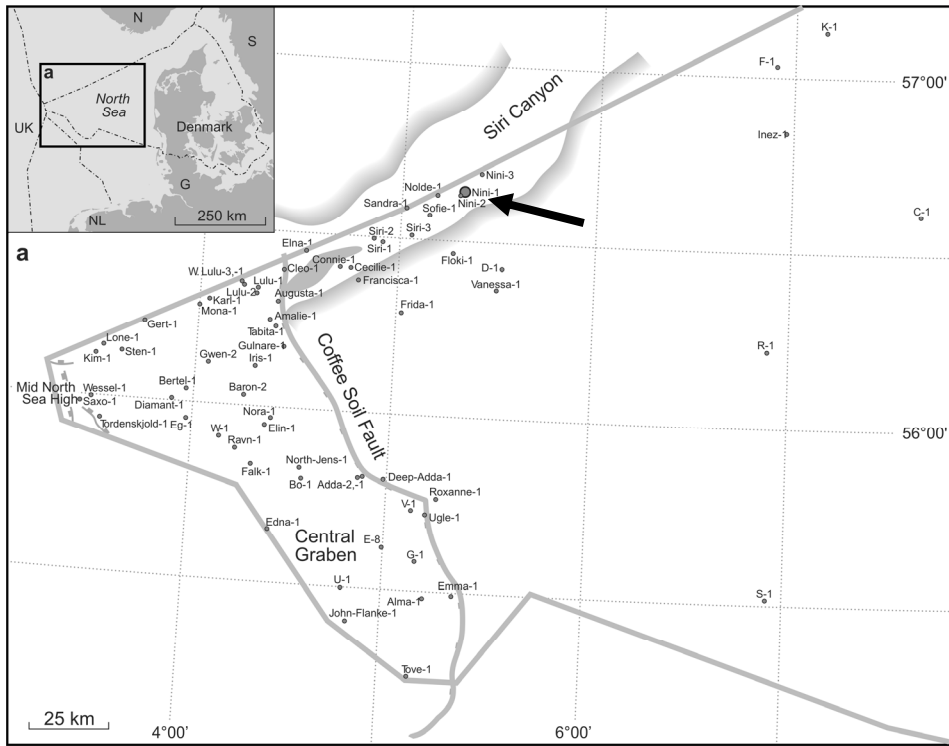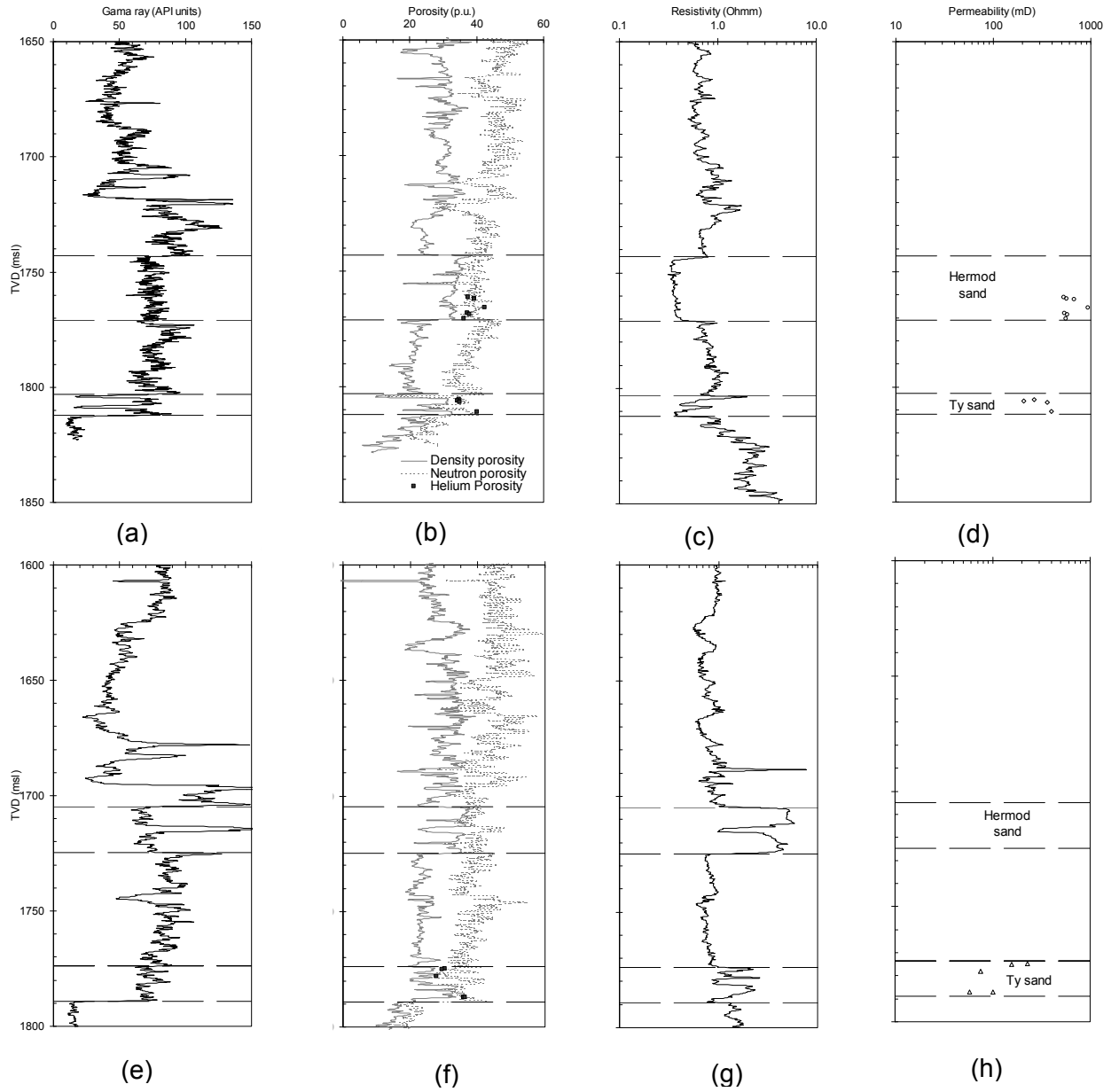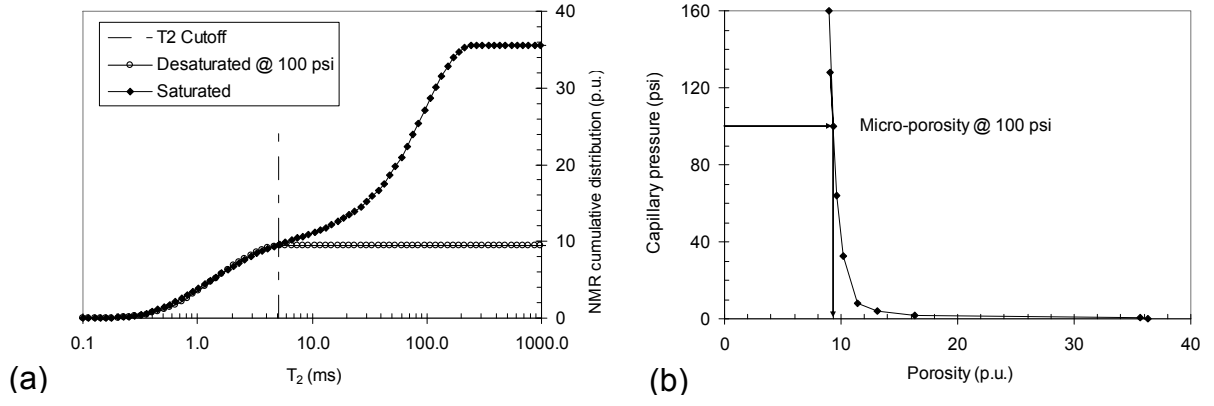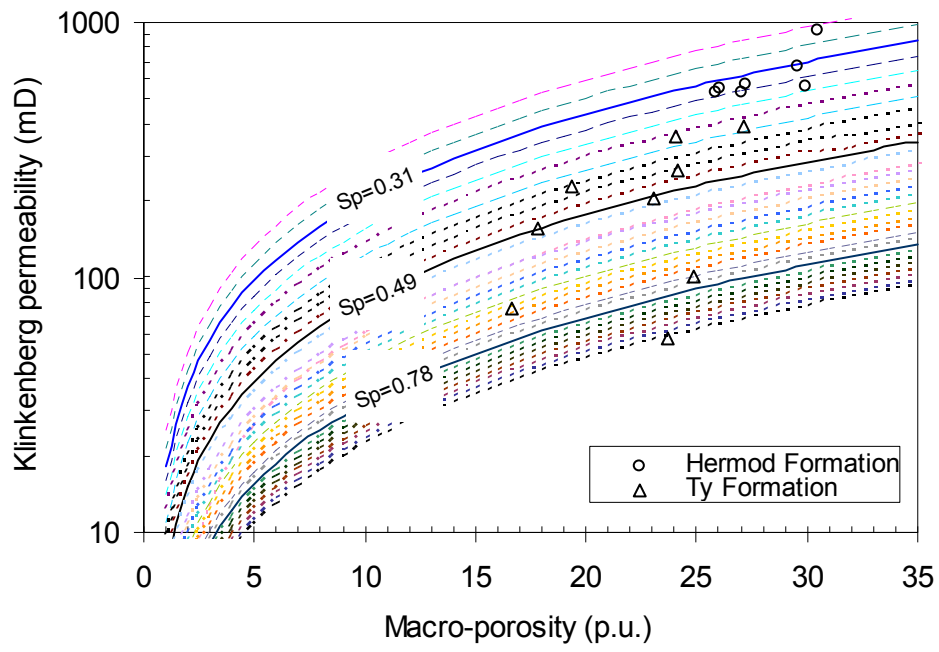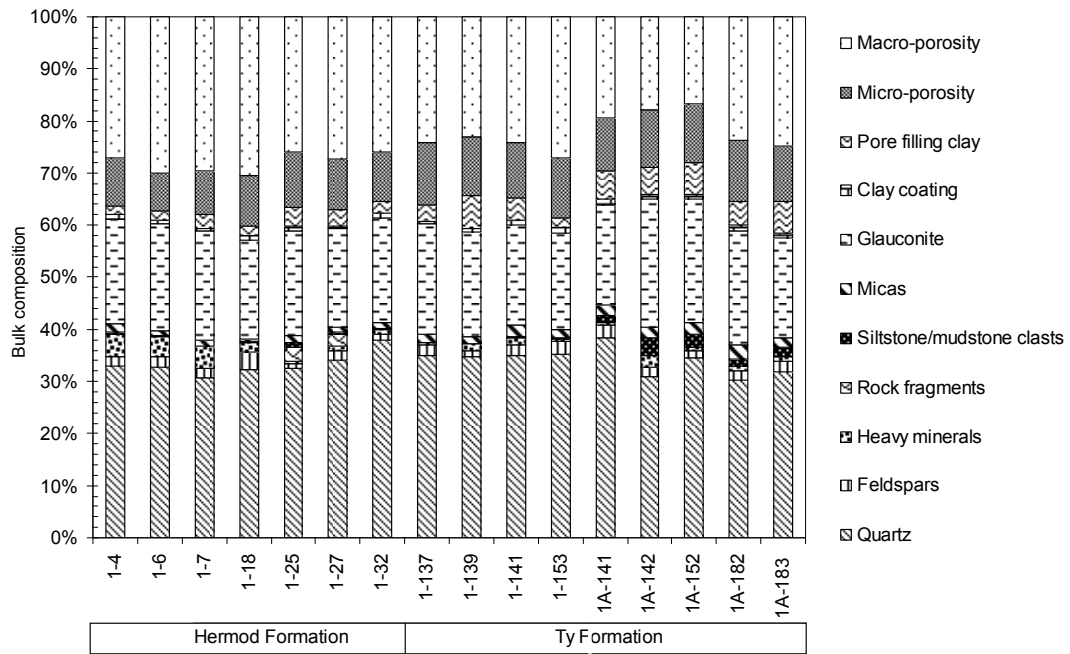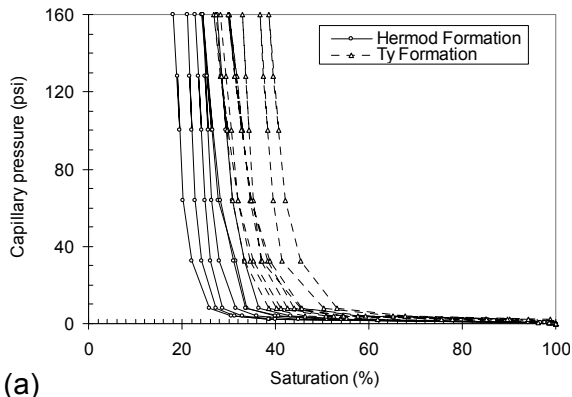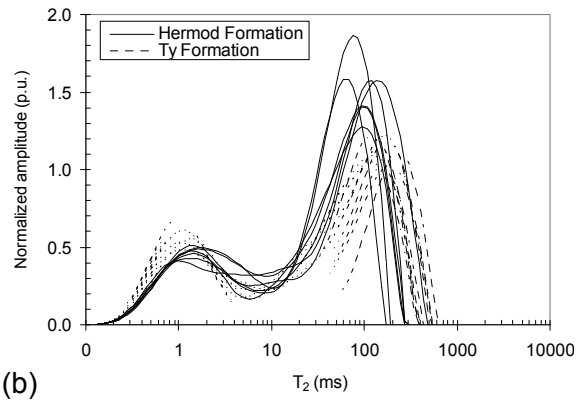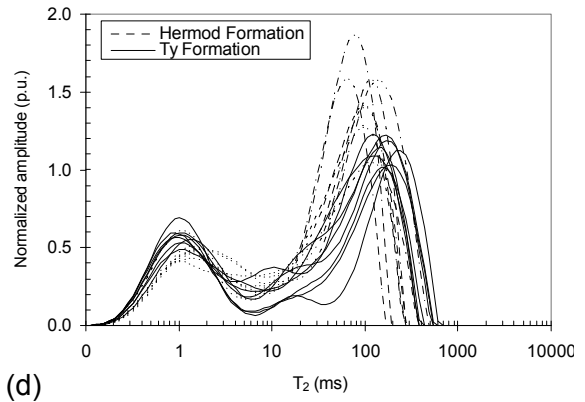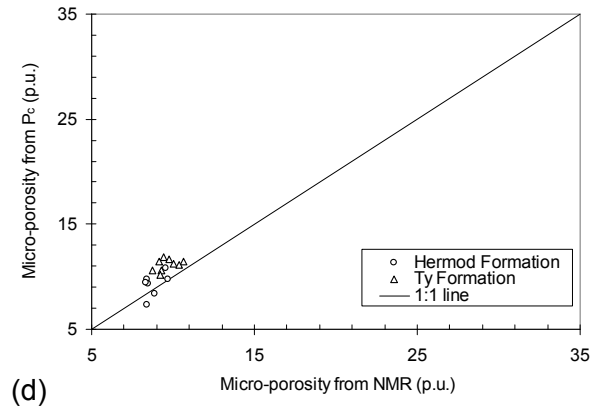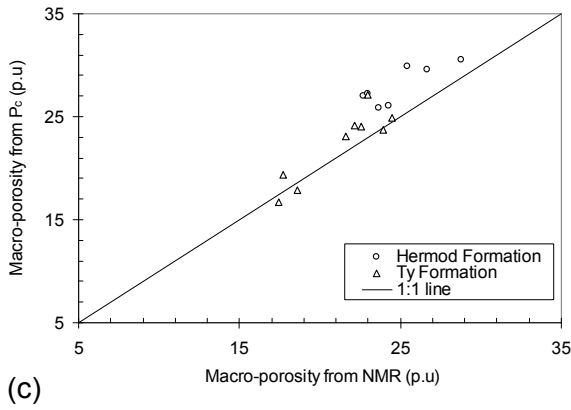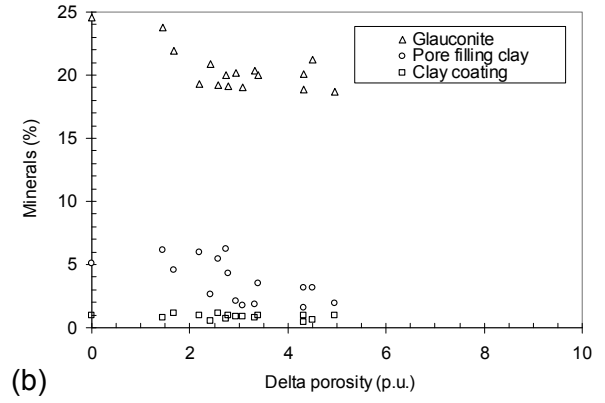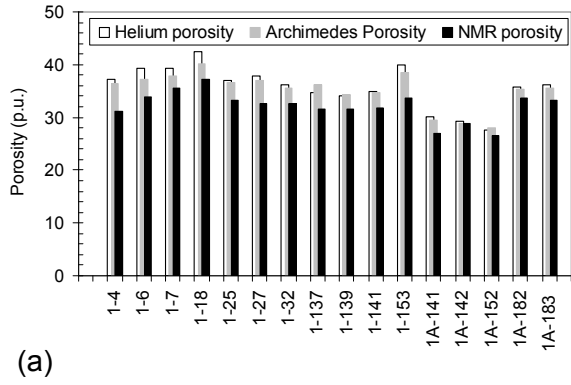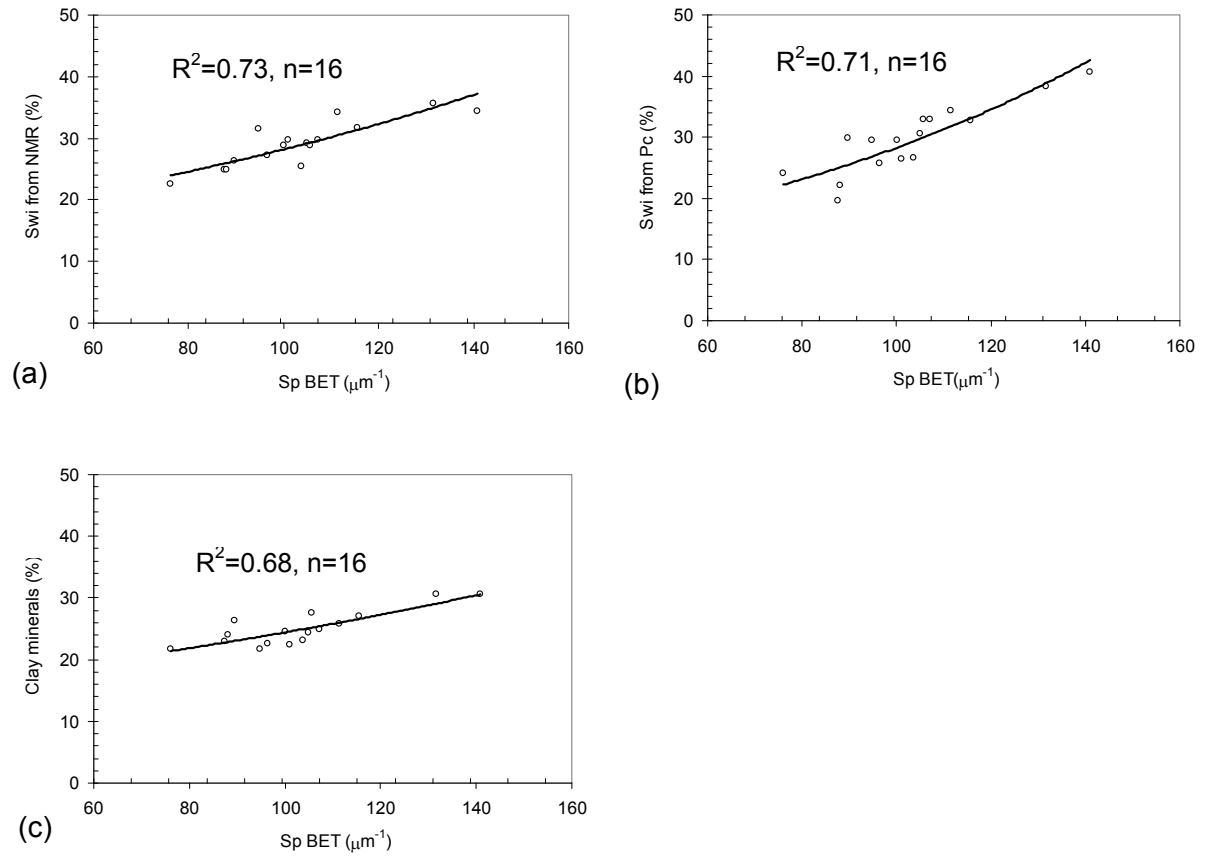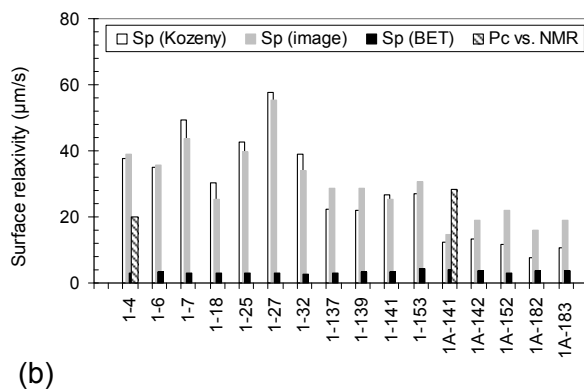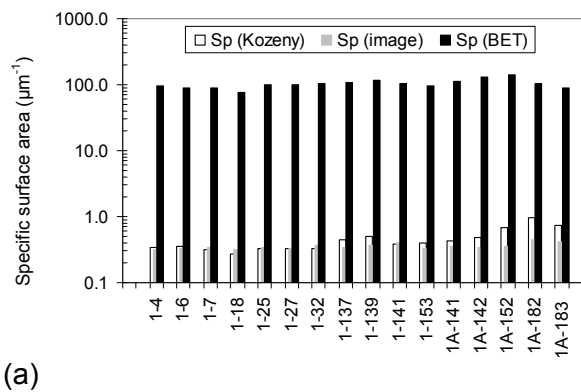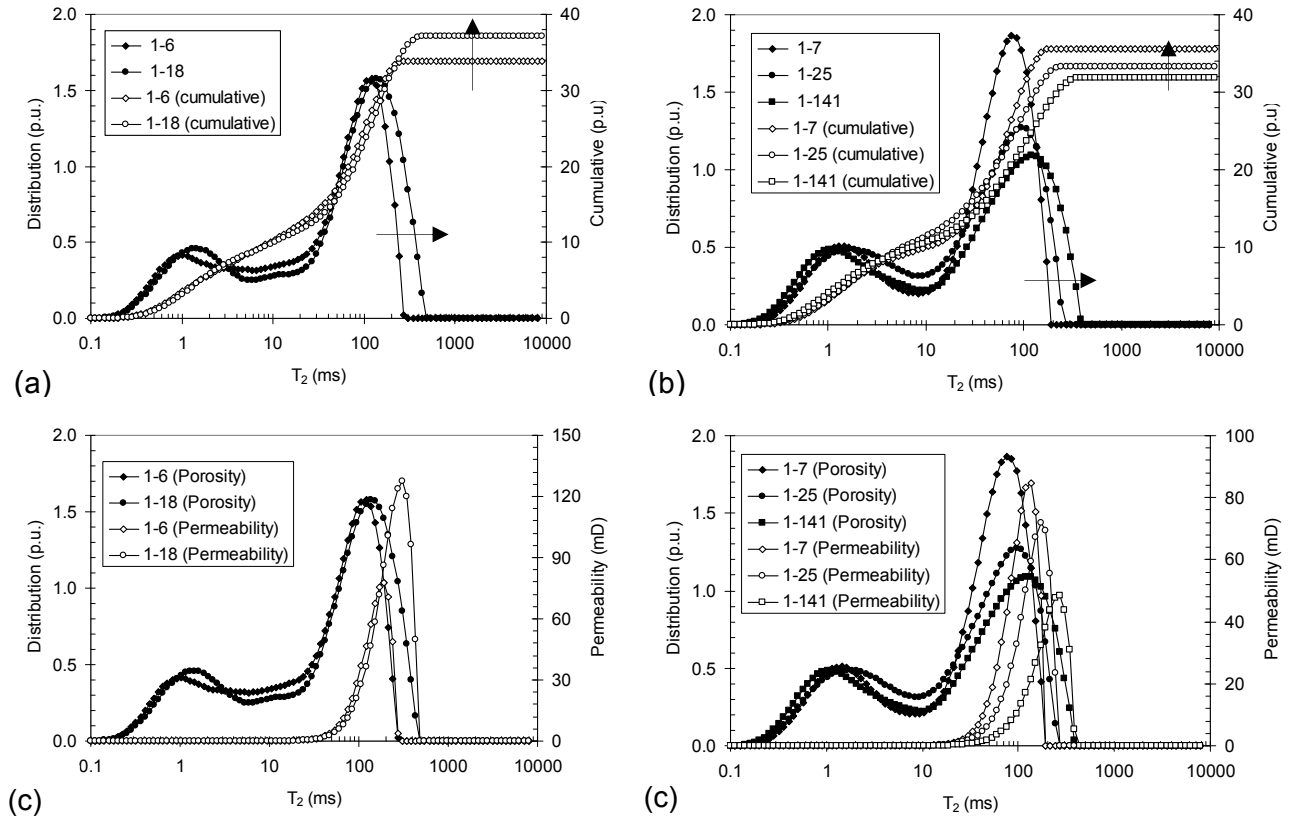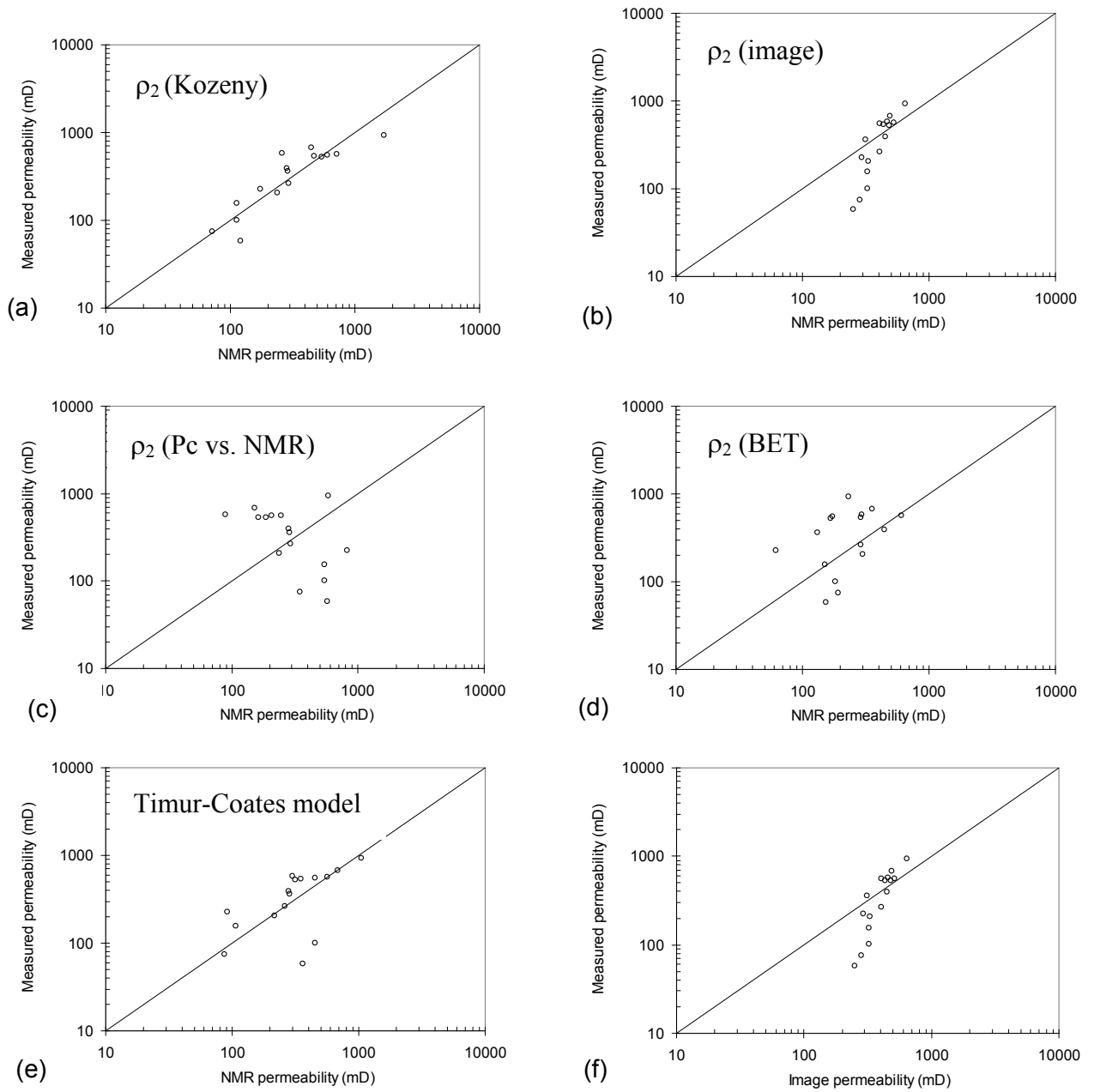
Fig. 13
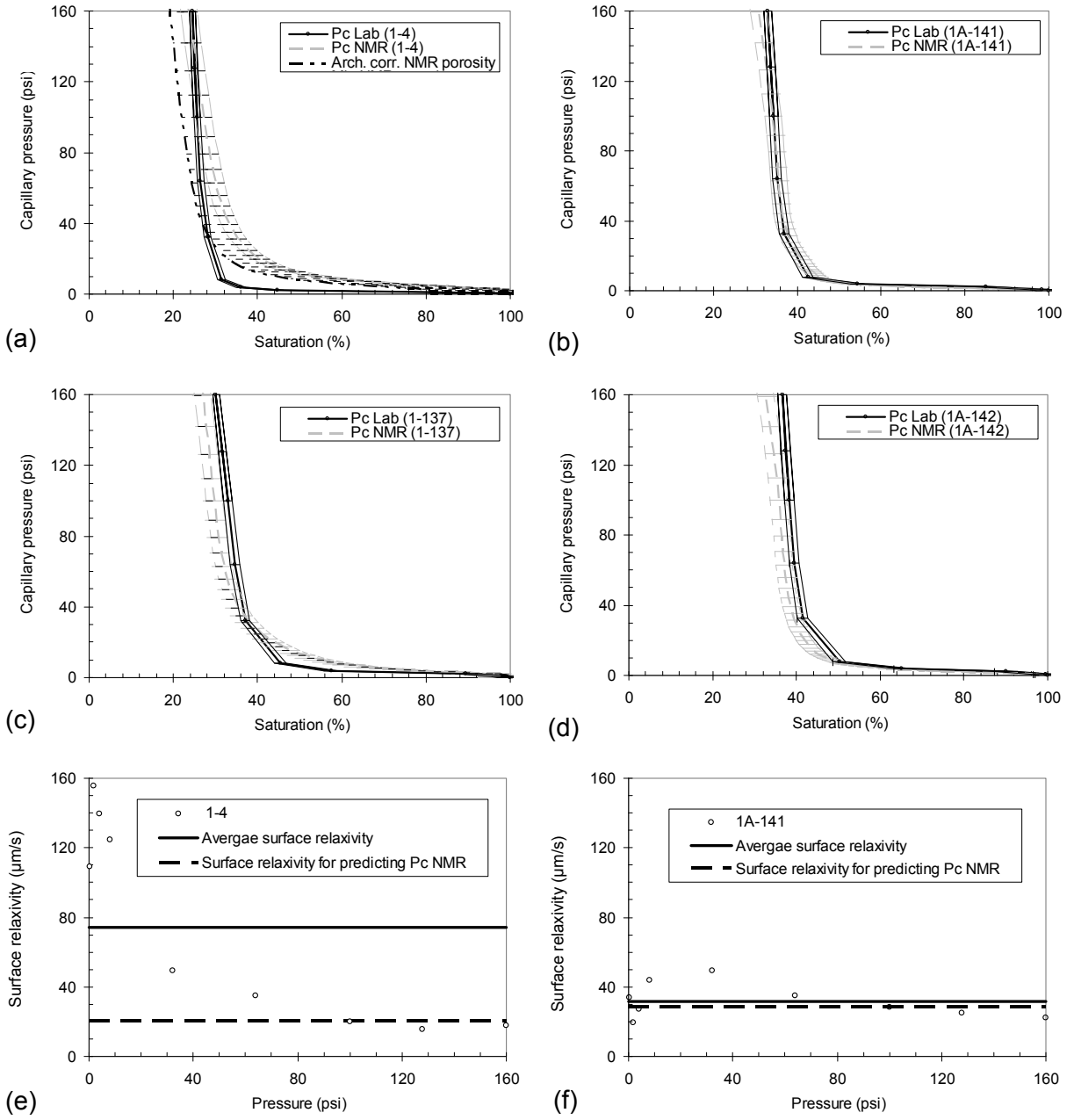
Table 1

Formation	Measured Depth (m)	TVD (msl)	Sample ID	Helium porosity (p.u.)	Error ±	Archimedes porosity (p.u.)	Error ±	NMR porosity (p.u.)	Error ±	Archimedes macro-porosity (p.u.)	NMR macro-porosity (p.u.)
Hermod	1761.1		1-4	37.3	1.5	35.5	1.1	31.2	0.4	27.0	22.7
	1761.7		1-6	39.3	1.3	37.2	1.1	33.8	0.5	29.9	25.4
	1762.1		1-7	39.2	0.4	37.9	1.1	35.5	0.5	29.6	26.7
	1765.7		1-18	42.4	0.5	40.2	1.2	37.2	0.5	30.5	28.8
	1768.1		1-25	37.1	0.5	36.7	1.1	33.3	0.5	25.9	23.7
	1768.7		1-27	37.8	1.1	37.0	1.1	32.7	0.5	27.2	23.0
	1770.4		1-32	36.2	0.9	35.5	1.1	32.6	0.5	26.0	24.3
Ty	1805.5		1-137	34.7	0.8	36.1	1.1	31.6	0.4	24.2	22.2
	1806.1		1-139	34.2	0.5	34.3	1.0	31.6	0.4	23.1	21.6
	1806.7		1-141	34.9	0.3	34.6	1.0	31.8	0.4	24.1	22.5
	1810.7		1-153	40.0	0.4	38.6	1.2	33.6	0.5	27.2	23.0
	1972.1	1774.7	1A-141	30.1	0.1	29.5	0.9	27.0	0.4	19.4	17.7
	1972.4	1775.0	1A-142	29.3	0.7	29.0	0.9	29.0	0.4	17.9	18.6
	1975.8	1778.1	1A-152	27.7	0.3	28.1	0.8	26.6	0.4	16.7	17.5
	1985.7	1787.0	1A-182	35.7	0.1	35.3	1.1	33.7	0.5	23.7	23.9
	1986.0	1787.2	1A-183	36.2	0.4	35.5	1.1	33.3	0.5	24.9	24.5

Table 2

Sample ID	Klinkenberg permeability (mD)	SSA (BET) (m²/g)	Sp (Kozeny) (μm⁻¹)	Sp (image) (μm⁻¹)	T₂ Cutoff (ms)	Irreducible water saturation from P_c (%)	Irreducible water saturation from NMR (%)
1-4	530	21	0.34	0.32	5.2	25.6	27.2
1-6	560	21	0.35	0.33		19.6	24.9
1-7	680	21	0.31	0.35		22.1	24.9
1-18	940	19	0.27	0.32		24.2	22.6
1-25	540	20	0.33	0.35		29.4	28.8
1-27	570	22	0.33	0.33		26.5	29.8
1-32	550	21	0.32	0.36		26.7	25.5
1-137	260	20	0.45	0.34		33.0	29.8
1-139	210	22	0.49	0.38		32.8	31.8
1-141	360	20	0.38	0.39		30.5	29.2
1-153	390	23	0.39	0.33		29.6	31.6
1A-141	230	17	0.43	0.35	3.7	34.4	34.2
1A-142	160	19	0.49	0.35		38.4	35.7
1A-152	80	20	0.68	0.36		40.7	34.4
1A-182	60	22	0.95	0.46		32.9	28.9
1A-183	100	19	0.74	0.41		29.9	26.4